Chu *et al. Journal of Nanobiotechnology* (2025) 23:197
https://doi.org/10.1186/s12951-025-03262-9

Journal of Nanobiotechnology

RESEARCH **Open Access**

Platelet hitchhiking vascular-disrupting agents for self-amplified tumor-targeting therapy

Hongyu Chu[1,2,3], Yajun Xu[2,3], Yuezhan Shan[1,2,3], Mengmeng Sun[4], Weidong Zhao[2,3], Xuedong Fang[1*], Na Shen[2,3*] and Zhaohui Tang[2,3*]

Abstract

The vascular-disrupting agent DMXAA (5,6-dimethylxanthone-4-acetic acid) exhibits potent anticancer activity by targeting tumor vasculature and activating immune responses via the cGAS-STING pathway. However, its clinical application is hindered by nonspecific targeting and significant cardiovascular toxicity. This study introduces a novel self-amplified tumor-targeting delivery system(P@NPPD)comprising azide-functionalized poly(ethylene glycol)-*b*-poly-[(*N*-2-hydroxyethyl)-aspartamide]-DMXAA (N_3-PEG-*b*-PHEA-DMXAA, NPPD) conjugated to DBCO modified platelets. Among them, NPPD was synthesized by conjugating DMXAA to N_3-PEG-*b*-poly-[(*N*-2-hydroxyethyl)-aspartamide] through esterification. This system enhances tumor-specific drug delivery while minimizing systemic toxicity. Leveraging the natural tumor-homing properties of platelets and the coagulation cascade, P@NPPD selectively targets exposed collagen at tumor sites, initiating a self-amplifying release of DMXAA. This approach achieved a 2.61-fold improvement in targeting efficiency and an 89.1% tumor suppression rate. In addition to improving drug accumulation at tumor sites, P@NPPD significantly activated local immune responses, enhancing therapeutic efficacy and safety. These findings underscore the potential of P@NPPD as a promising platform for cancer therapy.

Background

The continuous delivery of oxygen and nutrients through blood vessels is critical for tumor growth [1–4]. Accordingly, the tumor vasculature has emerged as a key therapeutic target, leading to the development of strategies such as tumor artery embolization, chemoembolization, vascular disruption, and vascular normalization therapies [5, 6]. DMXAA, a representative vascular-disrupting agent (VDA), selectively induces apoptosis in tumor vascular endothelial cells, rapidly obstructing nutrient transport and starving tumor tissues [7, 8]. Additionally, DMXAA activates the cGAS-STING pathway by directly binding to the STING protein in cells, which triggers TBK1 phosphorylation and IRF3 activation within the type I interferon (IFN) signaling pathway, thereby enhancing both innate and adaptive antitumor immune responses [9]. Subsequently, Weiss et al. also verified and utilized DMXAA to induce immune activation, promote T-cell tumor infiltration and activation, and result in tumor suppression [10, 11].

This dual mechanism of vascular disruption and immune activation positions DMXAA as a compelling

---

*Correspondence:
Xuedong Fang
fangxd@jlu.edu.cn
Na Shen
nshen@ciac.ac.cn
Zhaohui Tang
ztang@ciac.ac.cn
Full list of author information is available at the end of the article

Graphical abstract

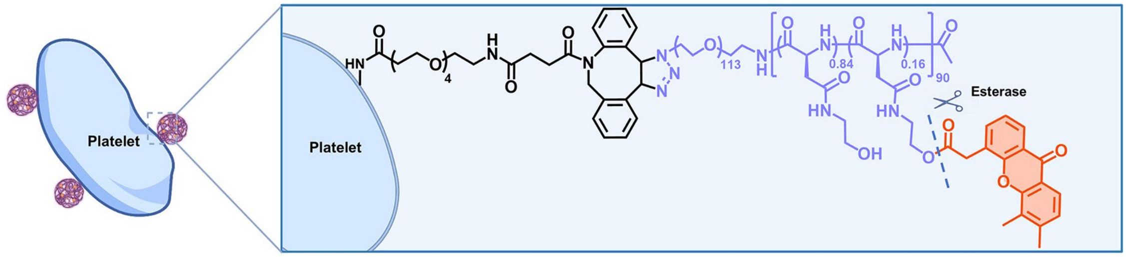

Keywords Self-amplified targeting, Vascular disrupting agent, DMXAA, Platelet-conjugated nanocarrier, Immune activation

candidate for cancer therapy. However, its clinical use is compromised by nonspecific targeting, which results in severe side effects, including cardiovascular toxicity, transient retinal impairment, and, in some cases, permanent apraxia [12]. These challenges necessitate the development of delivery systems that enhance tumor specificity while reducing off-target effects.

Efficient tumor-targeted drug delivery remains a significant challenge due to the complexities of the tumor microenvironment [13]. While drug-encapsulated nanomaterials show passive accumulation in tumors [14], their clinical efficacy is limited by high dense extracellular matrix barriers, intratumoral fluid pressure and complicated tumor microenvironment [15]. Active targeting strategies based on overexpressed tumor cell receptors have improved drug delivery but face limitations, as only 2% of nanoparticles successfully interact with tumor cells, with most remaining trapped extracellularly [16]. The scarcity and inaccessibility of traditional tumor-specific targets further complicate drug delivery efforts. To address these limitations, amplified tumor-targeting strategies have gained attention. These approaches leverage mechanisms like the self-amplifying coagulation cascade, which ensures rapid and effective responses to pathological conditions such as vascular damage [17–19]. For instance, Wang et al. developed a coagulation-targeting peptide-decorated poly($_L$-glutamic acid)-*graft*-maleimide poly(ethylene glycol)/combretastatin A4 conjugate (A15-PLG-CA4), which enhanced drug accumulation at tumor sites by 2.9-fold compared to a noncoagulation-targeting control [20]. These findings highlight the potential of self-amplifying delivery strategies to optimize vascular-disrupting agents for cancer treatment.

In recent years, cell-mediated delivery systems inspired by biological processes have garnered significant attention from researchers [21–24]. Among these systems, platelets have emerged as promising carriers for tumor-targeted drug delivery due to their natural affinity for subendothelial collagen [25, 26]. This characteristic is particularly relevant, as vascular systems undergo abnormal changes in size, shape, and structure during the progression of solid tumors [27, 28]. Moreover, clinical observations link elevated platelet counts (thrombocytosis) to newly diagnosed cancers [29, 30], and platelets can be efficiently isolated using advanced blood separation techniques [31]. These findings provide a robust foundation for the development of platelet-based drug delivery platforms. It is hypothesized that self-amplified tumor-targeted delivery can be achieved by hitchhiking vascular-disrupting agents like DMXAA onto platelets. This approach leverages platelets' ability to induce tumor vessel bleeding and initiate coagulation cascades, enabling targeted delivery through chemotaxis and enhanced tumor coagulation.

In this study, N_3-PEG-*b*-PHEA-DMXAA (NPPD) was synthesized by conjugating DMXAA with azide-poly(ethylene glycol)-*b*-poly-[(*N*-2-hydroxyethyl)-aspartamide] (N_3-PEG-*b*-PHEA, NPP) via esterification between carboxyl (-COOH) and hydroxyl (-OH) groups. Platelet-conjugated NPPD (P@NPPD) was then prepared through a click reaction between the azide groups of NPPD and the DBCO groups on functionalized platelets in vitro. The self-amplified tumor-targeted delivery was designed to proceed through the following cascade (Scheme 1): (1) P@NPPD actively targets tumors by adhering to exposed collagen in fast-growing tumor vasculature, releasing DMXAA in response to the tumor microenvironment. (2) Vascular disruption exposes additional collagen and coagulation signals, promoting further accumulation of P@NPPD. (3) This cascading effect drives targeted delivery of platelets to internal tumor vasculature, initiating a coagulation-targeted self-amplification process. (4) This amplification enhances DMXAA delivery to the tumor site. In vitro and in vivo experiments were conducted to evaluate whether P@ NPPD effectively targeted tumor vasculature, disrupted

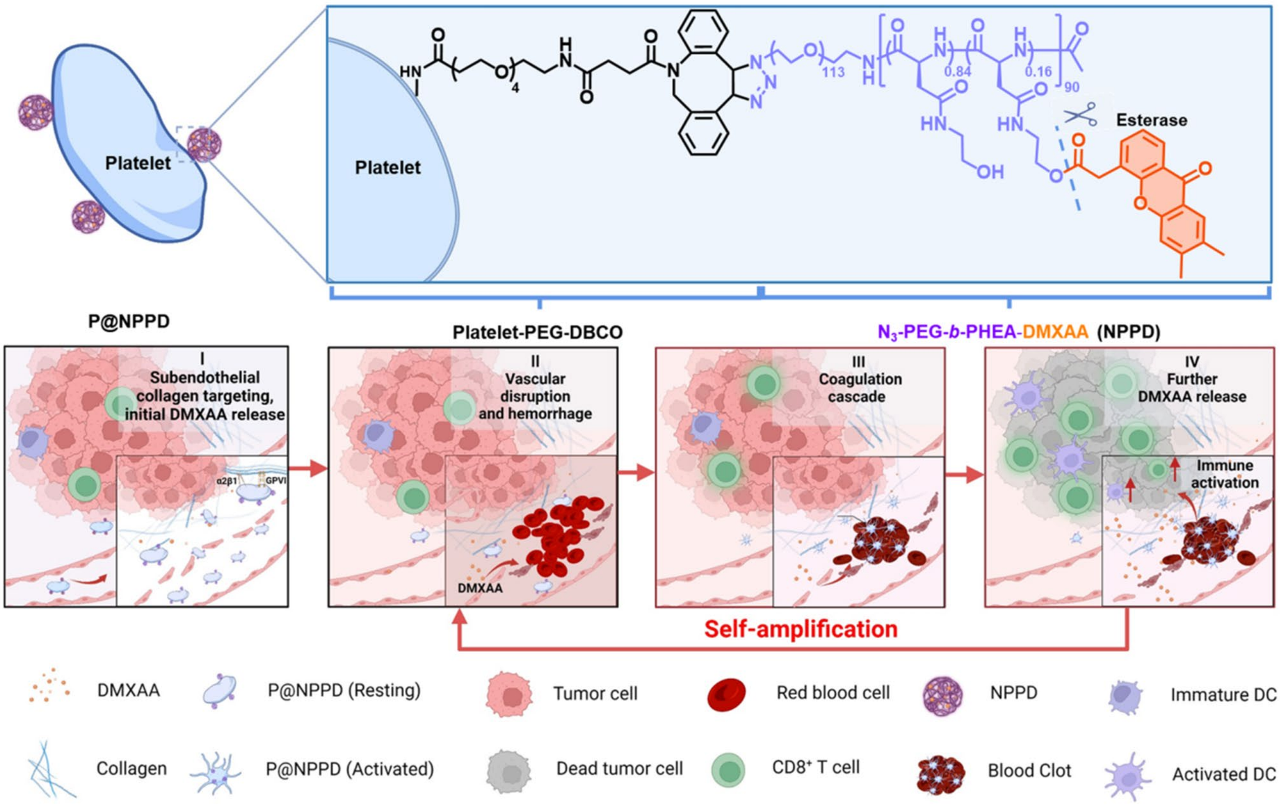

Scheme 1 Schematic image illustrating the design of self-amplified tumor-targeted delivery of platelet-hitchhiking DMXAA, involving the following steps: (1) Tumor Targeting: Upon intravenous administration, P@NPPD actively homes to tumors by binding to exposed collagen in the disrupted vasculature characteristic of fast-growing tumors. Leveraging the natural tumor-homing properties of platelets, this targeting mechanism ensures localized release of DMXAA, triggered by the unique conditions of the tumor microenvironment. (2) Vascular Disruption and Collagen Exposure: Once bound to the tumor vasculature, P@NPPD releases DMXAA, which disrupts tumor blood vessels. This vascular damage exposes additional collagen and coagulation signals, providing new binding sites for P@NPPD accumulation at the tumor site. (3) Cascade Amplification: The vascular disruption caused by DMXAA initiates a positive feedback loop, whereby platelet-mediated targeting drives further P@NPPD accumulation. This cascade effect significantly amplifies drug delivery efficiency, intensifying therapeutic impact on the tumor microenvironment. (4) Enhanced DMXAA Delivery and Immune Activation: The amplified accumulation of P@NPPD ensures efficient delivery of DMXAA. Beyond vascular disruption, DMXAA activates the STING pathway, stimulating the production of type I interferons and pro-inflammatory cytokines. This immune activation recruits immune cells, including $CD8^+$ T cells and dendritic cells, thereby reshaping the tumor immune microenvironment and enhancing tumor suppression

tumor blood vessels, enhanced biodistribution, promoted DMXAA release, and inhibited tumor growth. The findings demonstrated the potential of P@NPPD to improve drug delivery efficiency while minimizing systemic toxicity, providing a promising strategy for tumor vascular disruption therapy.

Materials and methods

Materials

γ-Benzyl-L-aspartate-*N*-carboxyanhydride (BLA-NCA) was obtained from Sichuan Jiaying Lai Technology Co., Ltd. (China). Anhydrous *N,N*-dimethylformamide (DMF, ≥ 99%) was sourced from Energy Chemical, while methanol was supplied by Adamas Pharmaceuticals, Inc. (Shanghai, China). DMXAA was purchased from Bide Pharmatech Co., Ltd. (Shanghai, China). Cy5-COOH and Cy5-NHS were procured from Wuhan Duofluor Inc. (Wuhan, China) and MeilunBio (Dalian, China), respectively. NHS-PEG4-DBCO was acquired from Xi'an Ruixi Biological Technology Co., Ltd. Additional reagents included N_3-PEG-NH_2 from Ponsure, N,N′-diisopropyl carbodiimide (DIC) from Aladdin, and 4-dimethylamino pyridine (DMAP) from Tokyo Chemical Industry.

CT26 cells and human umbilical vein endothelial cells (HUVECs) from Procell were used in this study. RPMI 1640 medium, penicillin, and streptomycin were supplied by MeilunBio (Dalian, China) and Seven (Shijiazhuang, China), respectively. Dimethyl sulfoxide (DMSO) was purchased from Glpbio (Montclair, CA). Antibodies, including β-actin (Cat. No. 20536-1-AP), TMEM173/STING (Cat. No. 66680-1-Ig), phospho-IRF3 (Cat. No. 29528-1-AP), and IRF3 (Cat. No. 11312-1-AP), were obtained from Proteintech (Wuhan, China). The phospho-STING (Ser366) monoclonal antibody (Cat. No. 19781) was sourced from Cell Signaling Technology (Massachusetts, USA). Rabbit anti-mouse CD4, CD8, CD31, CD11b, Ly6G, and CD11c antibodies were provided by Servicebio (Wuhan, China). Flow cytometry antibodies were obtained from BioLegend (California, USA), with details in Supplementary Table S2. All additional reagents and solvents were procured from Sinopharm Chemical Reagent Co., Ltd. (China).

Characterizations

The chemical structures of DMXAA, PPD, and NPPD were characterized using proton nuclear magnetic resonance spectroscopy (^{1}H NMR, Bruker AV-300) with CF_3COOD, DMSO-*d6*, or D_2O as solvents. Nanoparticle size and zeta potential were measured with a Zetasizer Nano ZS nanoparticle analyzer (Malvern, Shanghai Sibaiji Instrument System Co., Ltd.). Transmission electron microscopy (TEM) images were captured using a JEOL JEM-1011 microscope (Tokyo, Japan) at an accelerating voltage of 100 kV. For TEM, 10 μL of nanoparticle solution (0.5 mg/mL) was placed on a copper grid, and imaging was performed after solvent evaporation. Pharmacokinetic analysis was conducted using a Tecan Spark multimode microplate reader (Switzerland). Ultraviolet-visible (UV/Vis) spectra were recorded with a Lambda365 spectrometer (PerkinElmer, USA). Biodistribution studies utilized an IVIS Lumina LT series in vivo imaging system (PerkinElmer, USA). High-performance liquid chromatography (HPLC) analysis employed a reverse-phase C18 column (Supersil ODS2, 5 μm) with a UV-Vis detector. The mobile phase consisted of methanol and 0.1% trifluoroacetic acid (TFA) in water (9:1 ratio) at a flow rate of 1.0 mL/min, with detection at 345 nm.

Synthesis of the N_3-PEG-*b*-PBLA block copolymer

Using N_3-PEG-NH_2 as an initiator, the copolymer N_3-PEG-*b*-PBLA was synthesized through the ring-opening polymerization (ROP) of BLA-NCA. Initially, N_3-PEG-NH_2 (1.0 g, 0.2 mmol) was dehydrated using an azeotropic method with toluene. After evaporating the toluene under vacuum, N_3-PEG-NH_2 was dissolved in 80 mL of anhydrous DMF. Separately, BLA-NCA (4.96 g, 20 mmol) was dissolved in 60 mL of anhydrous DMF and carefully added to the N_3-PEG-NH_2 solution via pipette. The polymerization reaction was carried out at 25°C with continuous stirring for 48 h. Acetic anhydride (0.74 mL, 8 mmol) was subsequently added, and the reaction continued under the same conditions for an additional 24 h. The mixture was concentrated under reduced pressure, and N_3-PEG-*b*-PBLA was precipitated from DMF into glacial ether (yield: 82%).

To convert N_3-PEG-*b*-PBLA into N_3-PEG-*b*-PHEA, 2.6 g (0.1 mmol) of the copolymer was dissolved in 50 mL of dry DMF, followed by the addition of ethanolamine (5.92 mL). The mixture was stirred at 35°C for 24 h. The crude product, N_3-PEG-*b*-PHEA, was obtained by precipitating the reaction mixture into ice-cold diethyl ether and vacuum drying the resultant solid. Further purification involved dialysis (MWCO = 3500 Da) against distilled water, followed by lyophilization, yielding a purified product with 68%. The chemical structures of N_3-PEG-*b*-PBLA and N_3-PEG-*b*-PHEA were confirmed using ^{1}H NMR spectroscopy using CF_3COOD and D_2O as solvents, respectively.

Synthesis of NPPD

NPPD was synthesized via a condensation reaction between N_3-PEG-*b*-PHEA and DMXAA, using N, N′-diisopropylcarbodiimide (DIC) as the coupling agent and 4-dimethylaminopyridine (DMAP) as the catalyst. In a flame-dried flask, N_3-PEG-*b*-PHEA (0.53 g, 0.04 mmol), DMXAA (0.4 g, 1.4 mmol), and DMAP (174 mg, 1.42 mmol) were dissolved in 10 mL of dry DMF after 12 h under vacuum. DIC (0.16 g, 1.42 mmol) was added via syringe and reacted at 25°C for 24 h. The solution was precipitated in cold diethyl ether twice to remove unreacted DMXAA and impurities. The crude NPPD product was dried under vacuum, redissolved in DMF, and purified via dialysis against distilled water. The final purified product was lyophilized into a yellow solid. The drug loading (15.9%) and encapsulation efficiency (27.5%) of DMXAA in the NPPD conjugate were determined using UV-vis spectroscopy at 345 nm. The chemical structure of NPPD was confirmed using ^{1}H NMR spectroscopy with CF_3COOD as the solvent.

For drug-loading analysis, DMXAA loaded onto NPPD nanoparticles (NPs) was quantified using UV-vis spectroscopy. The drug loading content (DLC) and drug loading efficiency (DLE) were calculated using standard equations.

$$\mathrm{DLC}(\%) = \frac{\mathrm{m_{loaded\ drug}}}{\mathrm{m_{NPs}}} \times 100$$

$$\mathrm{DLE}(\%) = \frac{\mathrm{m_{loaded\ drug}}}{\mathrm{m_{feeding\ drug}}} \times 100$$

Where:

$M_{\text{loaded drug}}$: Mass of the drug successfully loaded into the nanoparticles.

M_{NPs}: Total mass of nanoparticles.

$M_{\text{feeding drug}}$: Mass of the drug initially used for loading.

Cy5-labeled NPPD was prepared by reacting NPPD (50 mg) with Cy5 (2.5 mg) in 2 mL of DMF at ambient temperature for 48 h under dark conditions. The resulting solution was purified via dialysis against distilled water and lyophilized, yielding Cy5-labeled NPPD as a dry powder, which was stored in the dark.

Preparation of NPPD-conjugated platelets (P@NPPD)

To introduce triple bonds into platelets for click chemistry, 1×10^8 platelets were incubated with 20 μM DBCO-PEG$_4$-NHS ester at room temperature for 30 min. Verification of triple-bond incorporation was performed by incubating the modified platelets with 50 μM azide-FITC for 30 min in the dark, followed by flow cytometry analysis (10^4 events collected).

For platelet-NPPD binding, platelets modified with DBCO and prestained with calcein AM were incubated with NPPD/Cy5 (2.2 mg/mL in 1 mL PBS, pH 7.4) at 37°C for 50 min. To neutralize remaining DBCO sites, 50 μM azide-PEG was added to the mixture, followed by 20 min of additional incubation. The resulting platelet@NPPD/Cy5 complexes were isolated via centrifugation at 1000× g for 10 min and analyzed using flow cytometry.

In vitro drug release study

Drug release was studied in vitro using PBS at pH 7.4. Precisely weighed NPPD powder was dissolved in 5.0 mL of the release medium, enclosed in a dialysis bag (MWCO = 3500 Da), and immersed in 45.0 mL of the same medium. The release of P@NPPD was also evaluated using this setup. To simulate a clot environment, fresh non-anticoagulated blood was used to form clots. P@NPPD was mixed with 1 mL of freshly collected non-anticoagulated blood and gently stirred to ensure uniform dispersion. The mixture was incubated at 37°C for 10 min to promote clot formation. Once the clot formed, excess serum was removed, and the clot containing P@NPPD was transferred into a dialysis bag (MWCO = 3500 Da). The release of DMXAA was quantified by high-performance liquid chromatography (HPLC), using an elution solvent composed of methanol and 0.1% trifluoroacetic acid in water (90:10, v/v).

The release study was conducted at 37°C with gentle agitation at 100 rpm in a thermostatic shaker. At predetermined intervals, 2 mL of the release solution was sampled and replaced with an equal volume of fresh medium.

Collagen binding experiment

The binding efficiency of NPPD to collagen was evaluated using collagen-coated plates incubated with NPPD/Cy5, calcein AM-labeled platelets, and P@NPPD/Cy5 solutions (with platelets also pre-stained with calcein AM). The plates were incubated at 37°C for 1 h, followed by thorough PBS washes to remove unbound particles or platelets. Fluorescence intensities of FITC and Cy5 were analyzed using confocal microscopy to determine binding efficiency for each condition.

Stability tests

The hydrodynamic size of P@NPPD was measured using a Malvern Zetasizer Nano ZS to assess particle stability. Measurements were taken daily over four days at room temperature to detect potential size changes indicative of instability or aggregation. The stability of NPPD/Cy5 conjugation with platelets was analyzed using flow cytometry by monitoring Cy5 fluorescence within the gated platelet population. Additionally, to evaluate whether NPPD/Cy5 detached from platelets and was internalized by other blood cells, P@NPPD/Cy5 was incubated with anticoagulated whole blood at 37°C. Samples were collected at 0 and 24 h, and Cy5 fluorescence was analyzed using confocal microscopy to assess nanoparticle distribution among non-platelet cells.

Cell cultures

CT26 cells or 4T1 cells were cultured in RPMI-1640 medium supplemented with 10% FBS, 50 U/mL penicillin, and 50 U/mL streptomycin at 37°C in a 5% CO$_2$ environment.

Cell viability

Platelet viability was assessed by incubating platelets and P@NPPD in 96-well plates at 37°C for 0, 1, 3, and 5 days. At each time point, 10 μL of CCK-8 was added and incubated for 2 h for detection. The cytotoxic effects of DMXAA, NPPD, and P@NPPD were evaluated in 3T3 and HUVEC cells. A total of 5,000 cells per well were seeded in 96-well plates and treated with various concentrations of DMXAA, NPPD, or P@NPPD after overnight attachment. Following 48 h of incubation, cell viability was determined using the CCK-8 assay,

Cell uptake

HUVEC cells were seeded in confocal dishes and incubated overnight for attachment. P@NPPD/Cy5 or NPPD/Cy5 was added and incubated for 24 h. After incubation, cells were washed twice with PBS to remove uninternalized particles and stained with DAPI to visualize nuclei. Nanoparticle endocytosis was observed using confocal microscopy, with Cy5 fluorescence indicating internalized particles.

Tube disruption assay

First, 50 μL of Matrigel (BD Bioscience) was seeded into a prechilled 96-well plate and allowed to polymerize at 37°C for 40 min. HUVEC cells were subsequently seeded at a density of 2×10^5 cells per well in 100 μL of culture medium. Following tube formation, the cells were treated with PBS, NPPD, or P@NPPD for 6 h. Tube structures were observed and documented using an inverted microscope at 0 and 6 h.

Western blot experiments

Cell and tumor samples were lysed in RIPA buffer with inhibitors, while tumor tissues were homogenized using a tissue grinder before centrifugation at 12,000 × g for 15 min to collect supernatants. Protein concentrations were measured, denatured, separated by SDS-PAGE, and transferred to PVDF membranes. Membranes were blocked, incubated with primary and secondary antibodies, and visualized using ECL reagents.

Animals

Female BALB/c mice (6–8 weeks old, 18–20 g) and SD rats (180–200 g) were obtained from Beijing Vital River Laboratory Animal Technology Co., Ltd. Xenograft tumor models were established by subcutaneous injection of 1×10^6 CT26 or 4T1 cells into the abdominal region of each mouse. In vivo antitumor studies were performed in mice bearing CT26 colorectal or 4T1 breast cancer cells, adhering to the Guide for the Care and Use of Laboratory Animals. All protocols were approved by the Animal Care and Use Committee of the Changchun Institute of Applied Chemistry, Chinese Academy of Sciences.

Immunofluorescence analysis

To evaluate the tumor-targeting capability of P@NPPD/Cy5, the compound was administered intravenously, and mice were euthanized 6 h post-injection. For vascular disruption studies, mice received intravenous treatments (PBS, DMXAA, NPPD, or P@NPPD). After 72 h, mice were euthanized, and xenograft tissues were fixed, embedded, and subjected to antigen retrieval. The primary antibody was applied overnight at 4°C, followed by secondary antibody labeling for 1 h. Nuclei were counterstained with DAPI and mounted. Nuclei were counterstained with DAPI and mounted using a fluorescent mounting medium. CD31 and colocalized P@NPPD/Cy5 with CD31 were visualized using a confocal microscope (Zeiss).

Tumor tissues were fixed overnight in 10% formalin, then transferred to 70% ethanol. Fixed samples were embedded in paraffin, sectioned, and stained with primary antibodies: rabbit anti-CD11c (GB11059, ServiceBio), anti-CD4 (GB15064, ServiceBio), anti-CD8 (GB15068, ServiceBio), anti-CD11b (GB11058, ServiceBio), and anti-Ly6G (GB11229, Servicebio). Slides were subsequently washed and incubated with secondary antibodies: HRP-conjugated goat anti-rabbit IgG (GB23303, ServiceBio), iF488-Tyramide (G1231, ServiceBio), CY3-Tyramide (G1223, ServiceBio), or Alexa Fluor 488-conjugated goat anti-rabbit IgG (ServiceBio).

Immunohistochemistry for CES2 staining

CT26 tumor tissues were paraffin-embedded, sectioned, and processed for antigen retrieval. After blocking, CES2 primary and HRP-conjugated secondary antibodies were applied, followed by DAB detection and hematoxylin counterstaining. CES2-positive signals appeared brown-yellow under the microscope.

Biodistribution analysis

A CT26 tumor model was established through subcutaneous injection into female BALB/c mice. Tumors were allowed to grow to 100–150 mm^3 before the mice were divided into groups for in vivo and ex vivo imaging. Mice received intravenous injections of NPPD/Cy5 or P@NPPD/Cy5. In vivo imaging was conducted using the IVIS Lumina LT Series III system at 3, 6, 12, and 24 h post-injection to evaluate nanoparticle accumulation at tumor sites. For ex vivo imaging, organs including the hearts, livers, lungs, kidneys, and tumors were harvested at 6, 12, and 24 h post-injection and imaged using the same system.

Pharmacokinetics study

Plasma pharmacokinetics were assessed in female SD rats treated with NPPD/Cy5 or P@NPPD/Cy5 (15 mg/kg DMXAA) via tail vein injection. Blood samples collected from 0.5 to 48 h post-injection were processed to obtain plasma and analyzed using a fluorescence microplate reader (excitation: 634 nm; emission: 681 nm). Pharmacokinetic parameters were calculated using PK solver software.

In vivo antitumor efficiency

Mice bearing tumors measuring 100–150 mm^3 were randomly assigned to treatment groups. Beginning on day 0, mice received intravenous injections of PBS, free DMXAA (15 mg/kg), NPPD (15 mg/kg DMXAA), or P@NPPD (15 mg/kg DMXAA) on days 0, 4, and 7. Tumor volumes were measured with vernier calipers to evaluate antitumor activity, while body weights were recorded to monitor systemic toxicity. Tumor volume and suppression rates were calculated using the formulas:

$$\mathrm{V}(\mathrm{mm}^3) = \frac{a \times b^2}{2} \tag{1}$$

$$\mathrm{TGI}\,(\%) \;=\; 1 - \frac{\mathrm{T}_{14} - \mathrm{T}_0}{\mathrm{V}_{14} - \mathrm{V}_0} \;\times 100\% \tag{2}$$

The measurements “a” and “b” correspond to the longest and shortest diameters of the tumor, respectively. T_{14} and T_0 indicate the tumor volume on days 14 and 0 in the treatment group, whereas V_t and V_0 denote the tumor volume on days 14 and 0 in the control group.

Hematoxylin-eosin (HE) staining analyses

At the end of treatments, mice were sacrificed, and organs and tumors were collected, fixed in 4% paraformaldehyde, embedded in paraffin, sectioned, and stained with H&E for histological analysis using a Nikon microscope.

Safety analysis

Peripheral blood was collected post-treatment via the medial canthus vein into EDTA-coated tubes for anticoagulation. Samples were stored at 4°C and centrifuged at 1000 × g for 20 min. Serum biochemical markers, including alanine aminotransferase (ALT), aspartate aminotransferase (AST), urea nitrogen (BUN), and creatinine (Cr), were measured.

Blood biochemistry and routine blood examination

On day 14, blood samples from healthy mice in all groups were analyzed for complete blood counts, including RBC, WBC, PLT, HGB, HCT, MCH, MCHC, and MCV, to assess potential myelosuppression.

In vivo immune response analysis

Tumors were harvested post-treatment for immune cell phenotyping via flow cytometry. Tumors were enzymatically digested at 37°C in a buffer containing collagenase, hyaluronidase, and deoxyribonuclease for 1 h, followed by filtration and centrifugation. Cell pellets were resuspended, stained with fluorophore-labeled antibodies, washed, and analyzed using a BD FACS Canto II flow cytometer. Antibody details are provided in Table S2 of the Supporting Information. Cytokine levels, including IFN-γ, TNF-α, IL-6, and vWF, were quantified using ELISA kits following the manufacturer's protocols.

Statistical analysis

Statistical analyses were performed with results expressed as means ± SDs. Two-group comparisons used a two-tailed unpaired Student's t-test, while one-way ANOVA with Tukey's multiple comparisons test was applied for multi-group analyses. Statistical significance was indicated as $^{*}p < 0.05$, $^{**}p < 0.01$, and $^{***}p < 0.001$. Survival analysis employed the Kaplan-Meier method with the log-rank test for significance evaluation.

Results and discussion

Preparation and characterization of the NPP and NPPD nanoparticles (NPs)

The synthesis of N_3-PEG-NH_2-based N_3-PEG-*b*-PHEA-DMXAA (NPPD) is depicted in Fig. 1a. N_3-PEG-***b***-PHEA (NPP) was selected as the carrier for its excellent biocompatibility and biodegradability. The N_3-PEG-*b*-PBLA copolymer was synthesized via controlled ring-opening polymerization (ROP) of γ-benzyl-L-aspartate-*N*-carboxyanhydride (BLA-NCA), initiated by N_3-PEG-NH_2 with an optimized amine/NCA molar ratio of 1:100. Subsequent ammonolysis with ethanolamine yielded N_3-PEG-*b*-PHEA. Structural integrity and composition were confirmed by ^1H NMR spectroscopy (Fig. 1b and S1), with quantitative analysis revealing 90 aspartic acid units, indicating the stability of poly(aspartic acid) during ammonolysis. ^1H NMR analysis further confirmed the successful conjugation of DMXAA to N_3-PEG-*b*-PHEA (Fig. 1c and S2), while UV spectroscopy validated the structural integrity of DMXAA post-conjugation (Fig. 1d). The conjugate exhibited a high DMXAA loading efficiency of 15.6% (Fig. S3). Morphological characterization via dynamic light scattering (DLS) and transmission electron microscopy (TEM) showed hydrodynamic diameters of 225.7 ± 24.1 nm for NPP and 238 ± 28.5 nm for NPPD. TEM images confirmed the uniform spherical morphology of NPPD, with an approximate diameter of 170 nm (Fig. 1e). NanoSight analysis confirmed the size of NPPD as 174 ± 62.5 nm, consistent with dynamic light scattering (DLS) measurements (Fig. S4, Fig. 1e). The sizes of platelets and P@NPPD were measured as 504.4 ± 35.0 nm and 600.9 ± 60.7 nm, respectively. The increase in the size of P@NPPD is due to the effective conjugation between NPPD NPs and platelets. Further, particle size stability tests showed no significant change in P@NPPD size over 4 days (Fig. S5). Conjugation stability of NPPD/Cy5 with platelets was assessed using flow cytometry and confocal microscopy. Results indicated that after 3 days in PBS, ~ 90% of NPPD/Cy5 remained conjugated to platelets (Fig. S6). Similarly, after 24 h co-incubation with anticoagulated blood, the majority of NPPD/Cy5 was still platelet-bound (Fig. S7). These findings confirm the robust stability of the NPPD/Cy5-platelet conjugation under both storage and physiological conditions.

NPP exhibited a negative zeta potential of -16.73 ± 0.12 mV, while NPPD showed a reduced negative charge of -5.92 ± 0.42 mV (Fig. S8). DMXAA release kinetics were evaluated in PBS to examine the impact of esterase. Without esterase (0 U/mL), NPPD exhibited a restrained release profile, with 11.66 ± 1.35% of DMXAA released over 72 h (Fig. 1f). In contrast, the addition of esterase (20 U/mL) significantly accelerated release, reaching 35.9 ± 3.00%, attributed to enzymatic hydrolysis of the ester bond. In the P@NPPD + esterase group, DMXAA release was 32.99 ± 5.91% at 72 h, similar to the NPPD + esterase group. Drug release was further tested under simulated blood clot conditions to mimic the tumor microenvironment (TME). Coagulated P@NPPD + esterase showed reduced release compared to NPPD + esterase, with 26.5 ± 4.30% released at 72 h, highlighting the enzyme-responsive release mechanism. These results underscore the potential of NPPD for targeted therapy by facilitating DMXAA release in the enzymatic milieu of the TME.

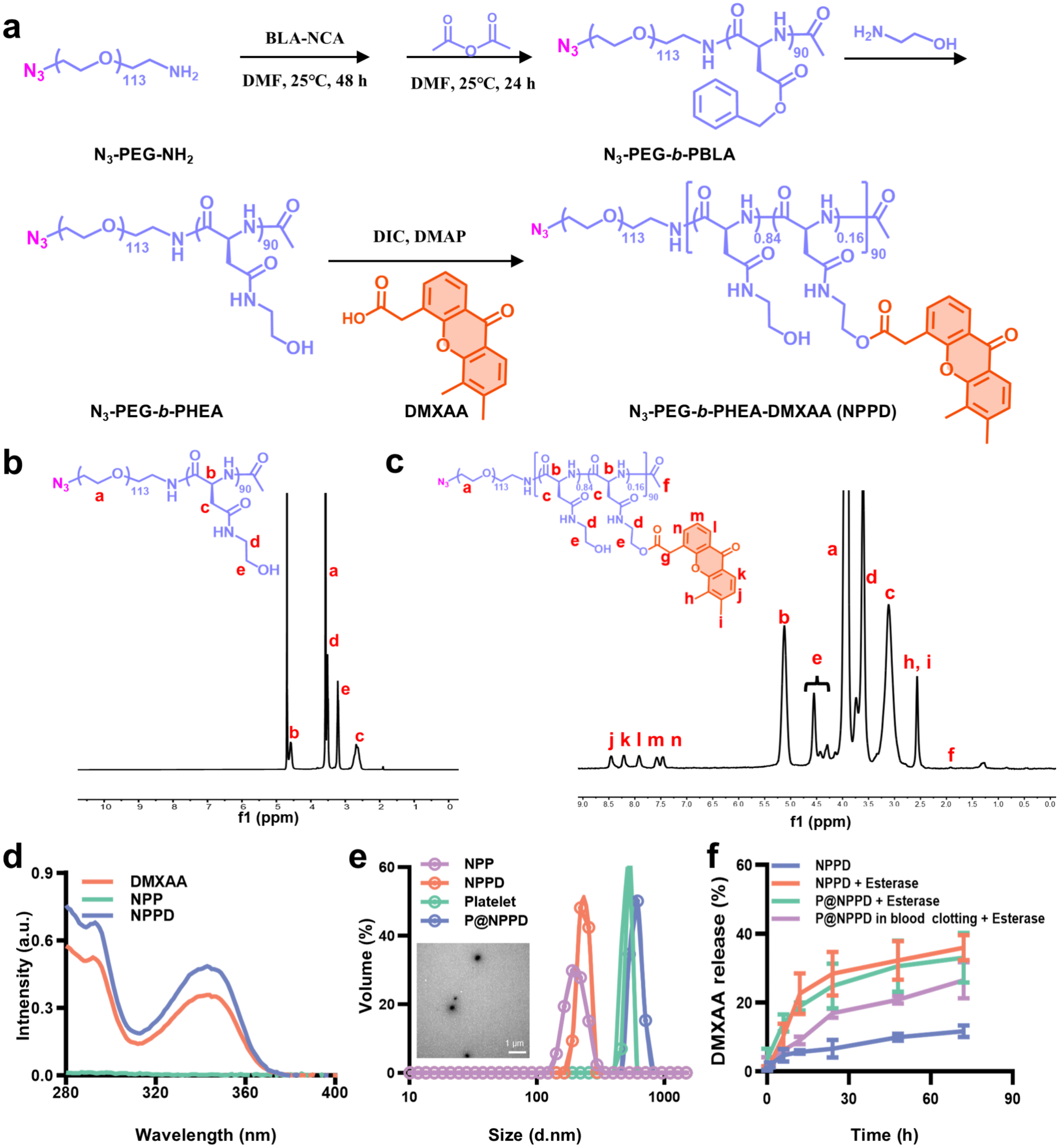

Fig. 1 Synthesis and physicochemical properties of N_3-PEG-*b*-PHEA-DMXAA (NPP). (**a**) Synthesis route of N_3-PEG-*b*-PHEA (NPP NPs) and its DMXAA conjugation to form NPPD. (**b**) ^{1}H NMR spectrum of N_3-PEG-*b*-PHEA in D_2O. (**c**) ^{1}H NMR spectrum of N_3-PEG-*b*-PHEA-DMXAA in CF_3COOH. (**d**) UV-vis spectra of DMXAA, NPP, and NPPD. (**e**) Hydrodynamic diameter of NPP, NPPDs, platelet, and P@NPPD in PBS, as assessed through dynamic light scattering (DLS). The morphology of NPPD is shown in the transmission electron microscopy (TEM) image (scale bar = 1 μm). (**f**) Release kinetics of DMXAA from NPPD, P@NPPD, and P@NPPD (in blood clotting) in PBS at pH = 7.4, with and without esterase (20 U/mL)

Integration and characteristics of NPPD with platelets

Platelets were isolated from mouse whole blood and treated with prostaglandin E1 (PGE1) to prevent activation [32]. The purity of isolated platelets was confirmed via routine blood analysis, showing no contamination by other blood cells (Table S1). The average platelet volume was 5.70 ± 1.64 fL, within the normal range for female BALB/c mice [33], confirming their morphological integrity (Table S1). For conjugation (Fig. 2a), platelets were

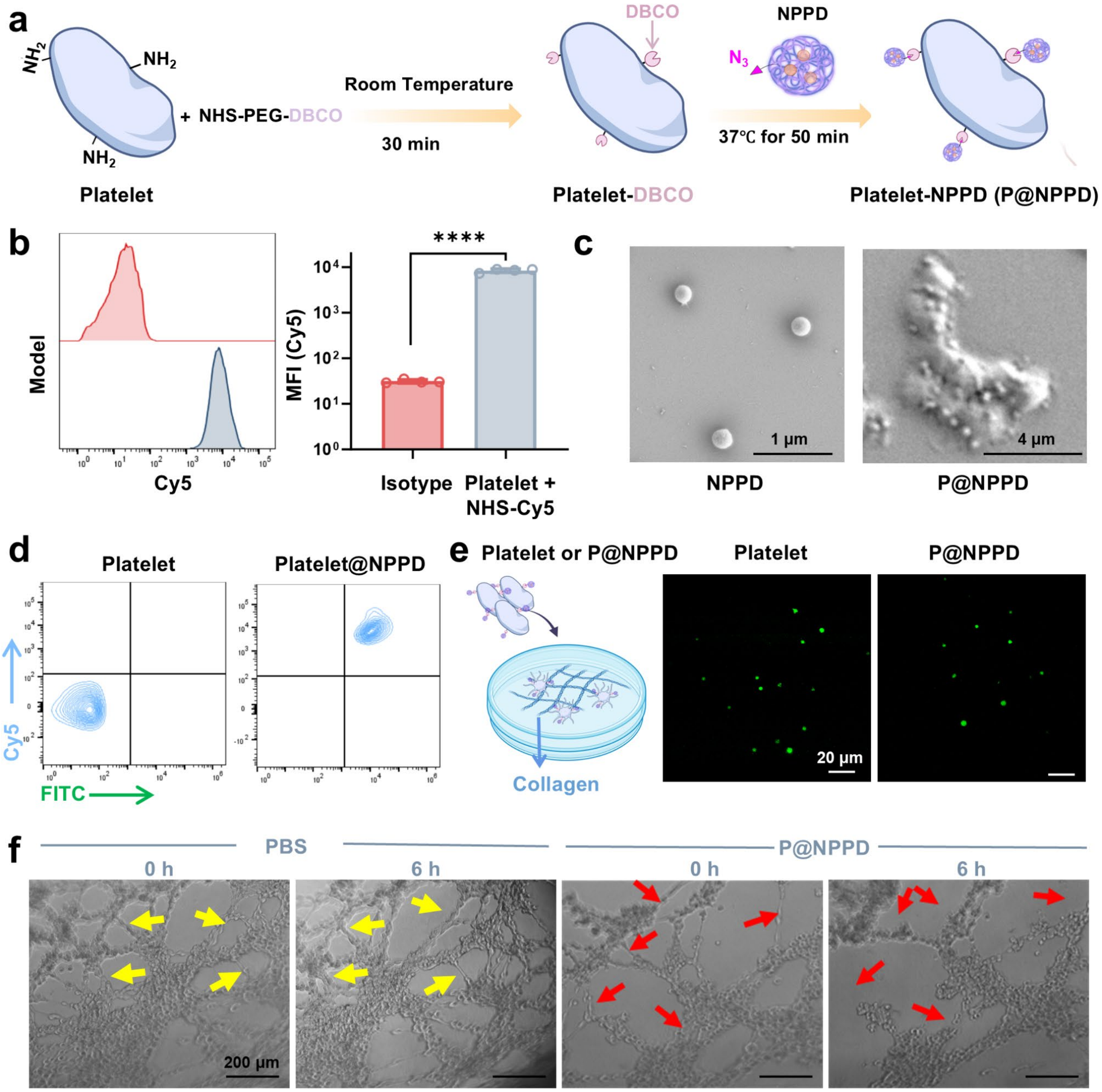

Fig. 2 Characterization of platelet-conjugated NPPD (P@NPPD). (**a**) Synthesis route of plate-conjugated NPPD (P@NPPD). (**b**) Flow cytometry analysis of the reaction between NH_2 on platelets and NHS/Cy5. (**c**) SEM images of NPPD (left) and P@NPPD (right); scale bar = 1 μm. (**d**) Flow cytometry analysis of the conjugation between NPPD/Cy5 and platelets (FITC-labeled). (**e**) Binding assay between platelets, P@NPPD, and collagen through confocal microscopy, scale bar = 20 μm. (**f**) Microtubule disruption assay with PBS and P@NPPD at 0 h and 6 h of observation under a microscope, scale bar = 200 μm

modified with dibenzocyclooctyne-PEG-*N*-hydroxysuccinimide ester (DBCO-PEG-NHS ester), which reacts with azide groups on NPPD surfaces [34]. Flow cytometry confirmed successful reaction between platelets and NHS-Cy5, with significantly higher fluorescence intensity compared to controls (Fig. 2b). Further validation using an azide probe (N_3-FITC) demonstrated increased fluorescence in modified platelets compared to untreated or physically mixed controls, confirming efficient DBCO functionalization (Fig. S9).

We incubated DBCO-modified platelets with NPPD for 50 min to achieve final conjugation. Scanning electron microscopy (SEM) confirmed the direct conjugation between platelets and NPPD (Fig. 2c). Flow cytometry analysis of FITC-labeled, DBCO-modified platelets reacted with NPPD/Cy5 revealed that nearly all platelets were associated with NPPD/Cy5 following centrifugation and washing (Fig. 2d), demonstrating successful conjugation.

Collagen, a critical factor for targeted blood vessel and platelet-collagen binding, is exposed at tumor sites due to abnormal blood vessel formation. GPVI, a key glycoprotein receptor on the platelet membrane, directly interacts with collagen, mediating platelet adhesion and activation [35]. To evaluate its targeting ability, we assessed the collagen-binding capacity of P@NPPD. Results showed no significant difference compared to untreated platelets, indicating that P@NPPD retained effective collagen-binding functionality (Fig. 2e, Fig. S10). Platelet viability remained approximately 80% after five days of incubation, with no significant differences observed between the Platelet and P@NPPD groups (Fig. S11). Thrombin activation induced significant CD62P expression in both the platelet and P@NPPD groups ($P < 0.05$), confirming preserved platelet functionality (Fig. S11). Flow cytometry analysis revealed morphological changes, with activated P@NPPD exhibiting larger SSC and FSC values, indicating effective activation (Fig. S12). The uptake of NPPD and P@NPPD by HUVEC cells was also evaluated. Both NPPD and P@NPPD were effectively internalized, significantly inhibiting HUVEC viability (Fig. S13). Furthermore, P@NPPD's disruption effect on HUVECs was demonstrated in a Matrigel-coated 96-well plate. While the PBS group showed no microtubule disruption, significant disruption occurred in the P@NPPD group, highlighting its ability to disrupt tumor vessels within the tumor microenvironment (Fig. 2f, Fig. S14). These findings confirm the potential of platelet-mediated delivery systems, such as P@NPPD, for targeted vascular disruption in tumors.

Biodistribution and pharmacokinetic analysis of NPPD and P@NPPD

Tumor growth relies on sufficient oxygen and nutrients, prompting tumors to accelerate angiogenesis and expose subendothelial collagen [36]. Studies have shown that platelets maintain tumor blood vessel integrity by adhering to collagen [37, 38]. Consequently, we evaluated P@NPPD's targeting ability. NPPD/Cy5 was prepared via a standardized method, and P@NPPD/Cy5 was intravenously injected into mice bearing subcutaneous CT26 tumors. Confocal microscopy confirmed that P@NPPD/Cy5 accumulated and colocalized with tumor vasculature 6 h post-injection (Fig. 3a), demonstrating effective tumor targeting. The tumor microenvironment, enriched with esterases [39], facilitates the hydrolysis of ester bonds and the release of DMXAA, which selectively induces apoptosis in tumor vasculature. This apoptosis triggers bleeding and activates the coagulation cascade [22]. Tumor blood vessels stained with CD31 following treatment revealed that P@DMXAA significantly reduced vascular density compared to DMXAA and NPPD, indicating its potent vascular disruption effects (Fig. 3b). Hematoxylin and eosin (HE) staining at 6 h post-intravenous injection of DMXAA, NPPD, or P@NPPD revealed extensive hemorrhagic sites in CT26 tumors, suggesting significant coagulation (Fig. S15). To assess P@NPPD's ability to target tumor-associated coagulation, NPPD was labeled with Cy5 and coinjected with fibrinogen-FITC into BALB/c mice bearing CT26 tumors. *Ex vivo* fluorescence imaging at 12 and 24 h showed that P@NPPD/Cy5 (red) localized predominantly around coagulation regions (green; Fig. 3c, Fig. S16). These results demonstrate that platelets efficiently direct NPPD/Cy5 to coagulation sites within tumors.

To assess the enhanced enrichment of P@NPPD/Cy5 at tumor sites due to bleeding and activation of the coagulation cascade, an in vitro imaging system (IVIS) was used to monitor mice injected with either NPPD/Cy5 or P@NPPD/Cy5. Tumor and primary organ samples were collected at 6, 12, and 24 h post-injection for analysis. It was observed that P@NPPD primarily accumulates in the livers, kidneys, and tumors, influenced by complex interactions between platelets and the body's immune and clearance systems. The liver, characterized by a rich presence of macrophages and components of the mononuclear phagocyte system (MPS), plays a crucial role in the clearance of foreign particles [40]. Despite the conjugation with platelets, some P@NPPD particles are still recognized and captured by the MPS, leading to their accumulation in the liver, facilitated by the organ's high blood flow. Similarly, the kidneys' high blood flow and filtration capacity might contribute to P@NPPD accumulation, with their vascular network enabling transient retention of nanoparticles [41]. Although the liver displayed prominent signals, the fluorescence intensity of P@NPPD/Cy5 in tumor tissues was significantly higher than that of NPPD/Cy5 and increased progressively over time (Fig. 3d). Quantitative analysis of tumor mean fluorescence intensity (MFI) revealed a 2.61-fold greater accumulation of DMXAA in mice treated with P@NPPD compared to NPPD after 24 h (Fig. 3e). Small animal in vivo imaging confirmed this trend, showing a 2.1-fold higher tumor accumulation of P@NPPD/Cy5 compared to NPPD/Cy5 (Fig. S17). The enhanced accumulation of P@NPPD in tumor tissues can be attributed to the targeting effects of platelets, which interact with the tumor microenvironment. Blood coagulation cascades activated by the tumor can further promote the localization of P@NPPD, enhancing its therapeutic efficacy. These findings highlight the ability of P@NPPD to target tumors and amplify drug delivery via coagulation-mediated mechanisms, thereby enhancing DMXAA accumulation at tumor sites.

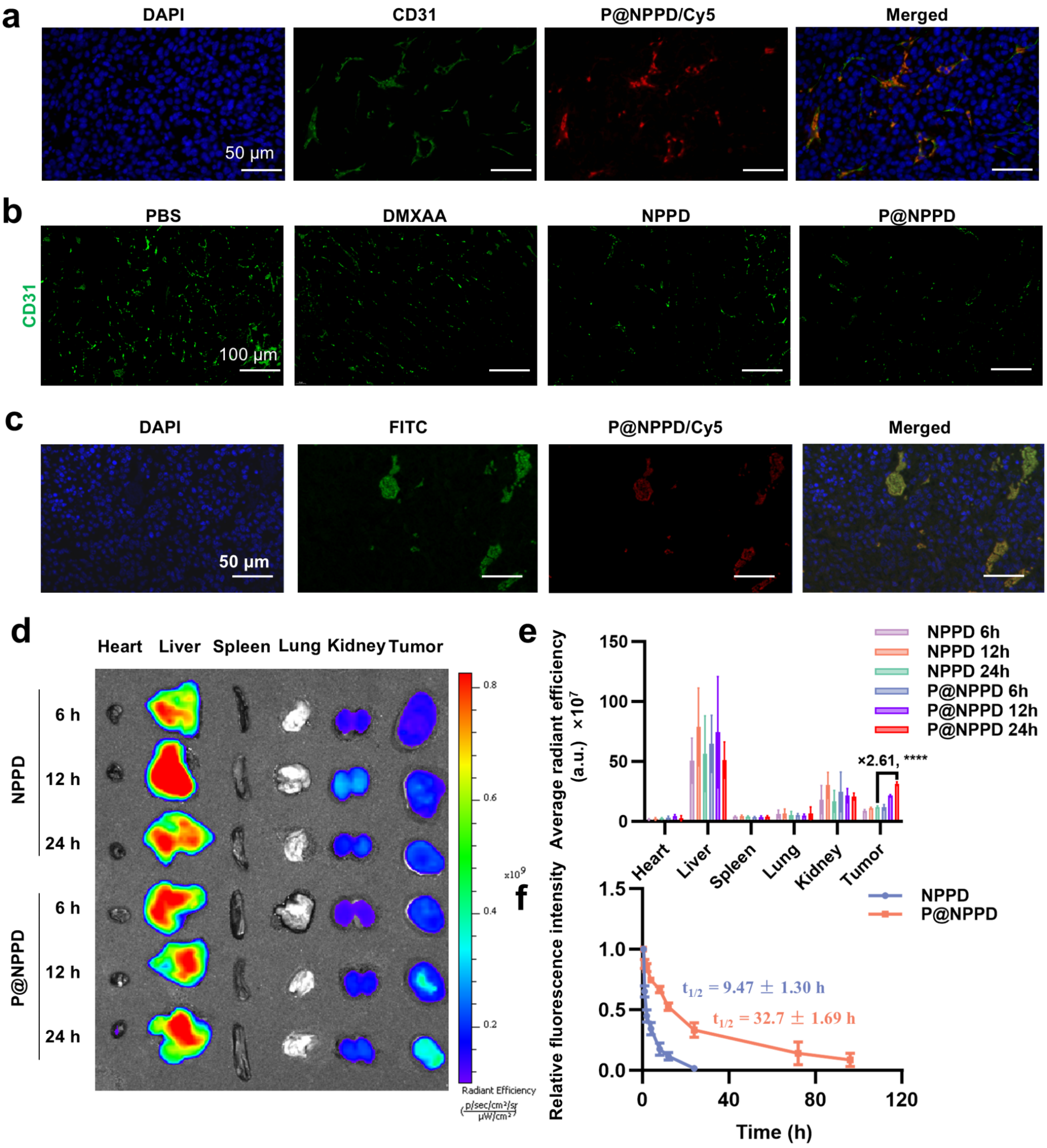

Fig. 3 Biodistribution of NPPD and P@NPPD in CT26 tumor-bearing mice. (**a**) CLSM images of tumor tissue sections treated with P@NPPD/Cy5. Green: CD31; red: Cy5; blue: DAPI. Scale bar: 50 μm. (**b**) CLSM images of tumor tissue sections treated with PBS, DMXAA, NPPD, or P@NPPD. Green: CD31, with a scale bar of 100 μm. (**c**) Histopathological examination of CT26 tumors 12 h after the administration of P@NPPD/Cy5 (equivalent to a dosage of 15.0 mg/kg DMXAA) and fibrinogen-FITC. The red Cy5-labeled NPPD was observed to cluster around the coagulation areas (marked in green), suggesting that the initial P@NPPD-induced hemorrhage at the tumor site likely led to the accumulation of more P@NPPD at the clotting zones. Scale bar: 50 μm. (**e**) Quantitative fluorescence assessment of the tissues shown in Fig. 3d was performed. The results are expressed as the mean ± S.D. (*n* = 3). (**f**) Fluorescence intensity was used to evaluate the half-life of NPPD/Cy5 and P@NPPD/Cy5 (*n* = 3)

The pharmacokinetics of NPPD/Cy5 and P@NPPD/Cy5 were also evaluated by measuring fluorescence intensity in the plasma of SD rats. NPPD/Cy5 was rapidly cleared from circulation, with a half-life of 9.47 ± 1.30 h. In contrast, P@NPPD/Cy5 exhibited a significantly prolonged half-life of 32.7 ± 1.69 h, which is approximately three times longer than NPPD/Cy5 (Fig. 3f). These results demonstrate that P@NPPD extends the circulation time of NPPD, thereby supporting long-lasting targeting efficacy.

Antitumor efficacy of P@NPPD in a CT26 tumor model

Encouraged by these promising results, the antitumor effects of P@NPPD were evaluated in CT26 tumor-bearing mice. Western blot and immunohistochemistry (IHC) analyses revealed higher esterase expression in CT26 tumor cells compared to mouse fibroblasts (Fig. S18). Following 48 h of incubation with DMXAA, NPPD, or P@NPPD, CT26 cell viability significantly decreased in the NPPD and P@NPPD groups (Fig. S19). Notably, 3T3 cells exhibited markedly lower cytotoxicity, indicating that P@NPPD preferentially targets tumor cells while minimizing toxicity to normal cells (Fig. S17). These results suggest that the elevated esterase levels in CT26 cells efficiently hydrolyze ester bonds, enabling effective drug release. Von Willebrand factor (vWF), a biomarker of cardiovascular toxicity, was assessed 24 h after treatment. Both NPPD and P@NPPD significantly reduced vWF levels compared to DMXAA, indicating reduced endothelial toxicity (Fig. S20). When tumor volumes reached 100–150 mm^3, mice were treated with PBS, DMXAA, NPPD, or P@NPPD (DMXAA dose: 15 mg/kg) (Fig. 4a). In the PBS group, tumors grew to 1500 mm^3 by day 14. DMXAA and NPPD inhibited tumor growth to varying extents, with tumor suppression rates (TSRs) of 45.33% and 74.37%, respectively (Fig. 4b, Fig. S21). Notably, P@NPPD demonstrated superior antitumor efficacy, achieving a TSR of 89.1%, and significantly reduced tumor size compared to other groups on day 14 (Fig. 4c). Additionally, P@NPPD treatment extended survival time more effectively than the other treatments (Fig. 4d).

Hematoxylin and eosin (HE) staining revealed that P@NPPD induced apoptosis in CT26 tumor tissues without causing significant damage to major organs (heart, liver, lungs, and kidneys; Fig. 4e and S22). Physiological evaluations showed a marked decrease in body weight following DMXAA administration, particularly on the first day post-treatment. In contrast, mice treated with NPPD or P@NPPD experienced minimal weight fluctuations, suggesting that these formulations mitigate the toxicity typically associated with DMXAA (Fig. 4f). Liver and kidney function tests revealed elevated levels of all measured parameters in the DMXAA group, indicating hepatic and renal impairment (Fig. S23). In contrast, the NPPD and P@NPPD groups maintained stable parameter levels, demonstrating that these treatments markedly reduce the toxicity associated with DMXAA. Routine blood tests conducted on day 14 showed no significant differences among groups, confirming that the therapeutic efficacy of NPPD and P@NPPD interventions does not compromise hematological safety (Fig. 4g). These findings highlight P@NPPD as a promising treatment with an optimal safety profile.

P@NPPD activates antitumor immunity

Given the role of DMXAA as a STING agonist [10], we evaluated the effects of P@NPPD on the tumor immune microenvironment using flow cytometry. In CT26 tumor-bearing mice, P@NPPD treatment significantly increased the proportions of $CD3^+CD8^+$ T cells and $CD3^+CD4^+$ T cells within tumors across all DMXAA-based groups (Fig. 5a and b) [42]. Notably, P@NPPD elicited the greatest enhancement in $CD3^+CD8^+$ T cell infiltration, with a 1.50-fold increase over the NPPD group and a 3.05-fold increase over the DMXAA group (Fig. 5a and b; gating strategy in Fig. S24).

Further analysis revealed that both DMXAA and NPPD treatments increased M1 macrophages ($CD11b^+F4/80^+CD80^+$) and the M1/M2 macrophage ratio, consistent with previous findings linking STING activation to M2-to-M1 macrophage repolarization [43]. P@NPPD demonstrated superior polarization capacity, outperforming DMXAA and NPPD by 1.74- and 1.47-fold, respectively (Fig. 5c and d; gating strategy in Fig. S25). Additionally, P@NPPD strongly promoted dendritic cell (DC) maturation (Fig. 5e; gating strategy in Fig. S26), suggesting its potential to reverse the immunosuppressive tumor microenvironment (TME) and enhance antitumor immunity. Although P@NPPD reduced myeloid-derived suppressor cell (MDSC) numbers compared to PBS controls, the reduction was not statistically significant (Fig. 5f; gating strategy in Fig. S27). Immunofluorescence analyses confirmed the flow cytometry results, illustrating consistent immune cell changes within the TME (Fig. S28-S30). Mechanistically, DMXAA-induced STING activation was associated with vascular disruption, tumor hemorrhage, and necrosis, alongside phosphorylation of STING and IRF3 proteins. This activation facilitated T cell infiltration and M1 macrophage polarization, reshaping the immune microenvironment and bolstering the antitumor response (Fig. S31). Encouraged by these results, we extended the evaluation to the 4T1 animal model. By the end of treatment, the P@NPPD group achieved an 81.3% tumor inhibition rate (Fig. S32). These findings demonstrate that P@NPPD effectively activates dendritic cells, polarizes macrophages, and recruits $CD4^+$ and $CD8^+$ T cells into tumors, collectively reshaping the tumor immune

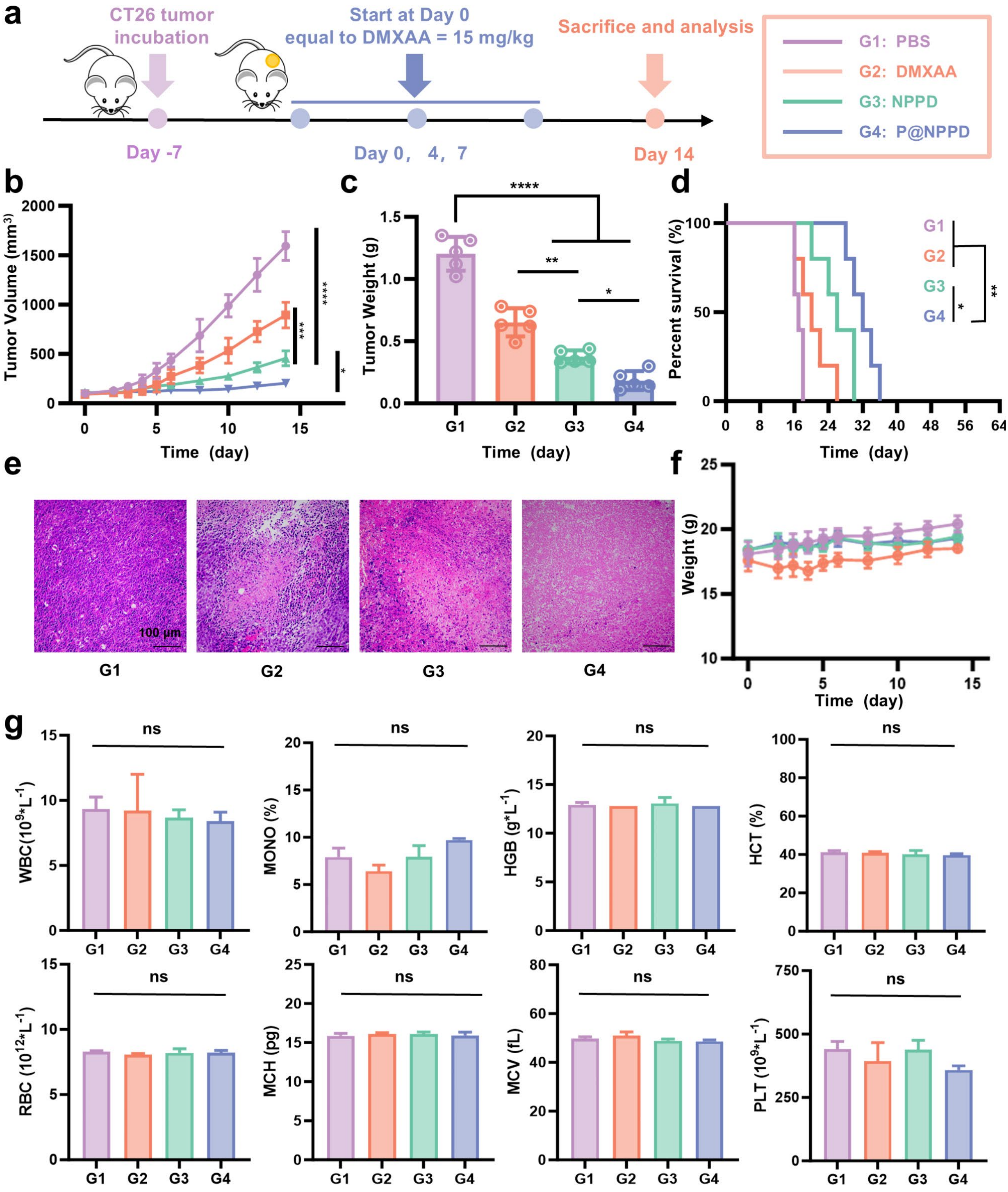

Fig. 4 Antitumor efficacy of P@NPPD in a CT26 tumor-bearing mouse model. (**a**) Schematic of the experimental design for the CT26 tumor model. (**b**) Tumor growth in CT26 tumor-bearing mice after different treatments were administered. (**c**) Average tumor weights for each group at the end of the study. (**d**) Survival curves showing the outcomes during the treatment period. (**e**) Histological analysis (HE staining) of tumors in each group after treatment, scale bar = 100 μm. (**f**) Changes in body weight observed during the treatment period. (**g**) Hematological parameters of the mice assessed 14 days after treatment. $^{*}p<0.05$, $^{**}p<0.01$, $^{***}p<0.001$, $^{****}p<0.0001$. Scale bar = 40 μm

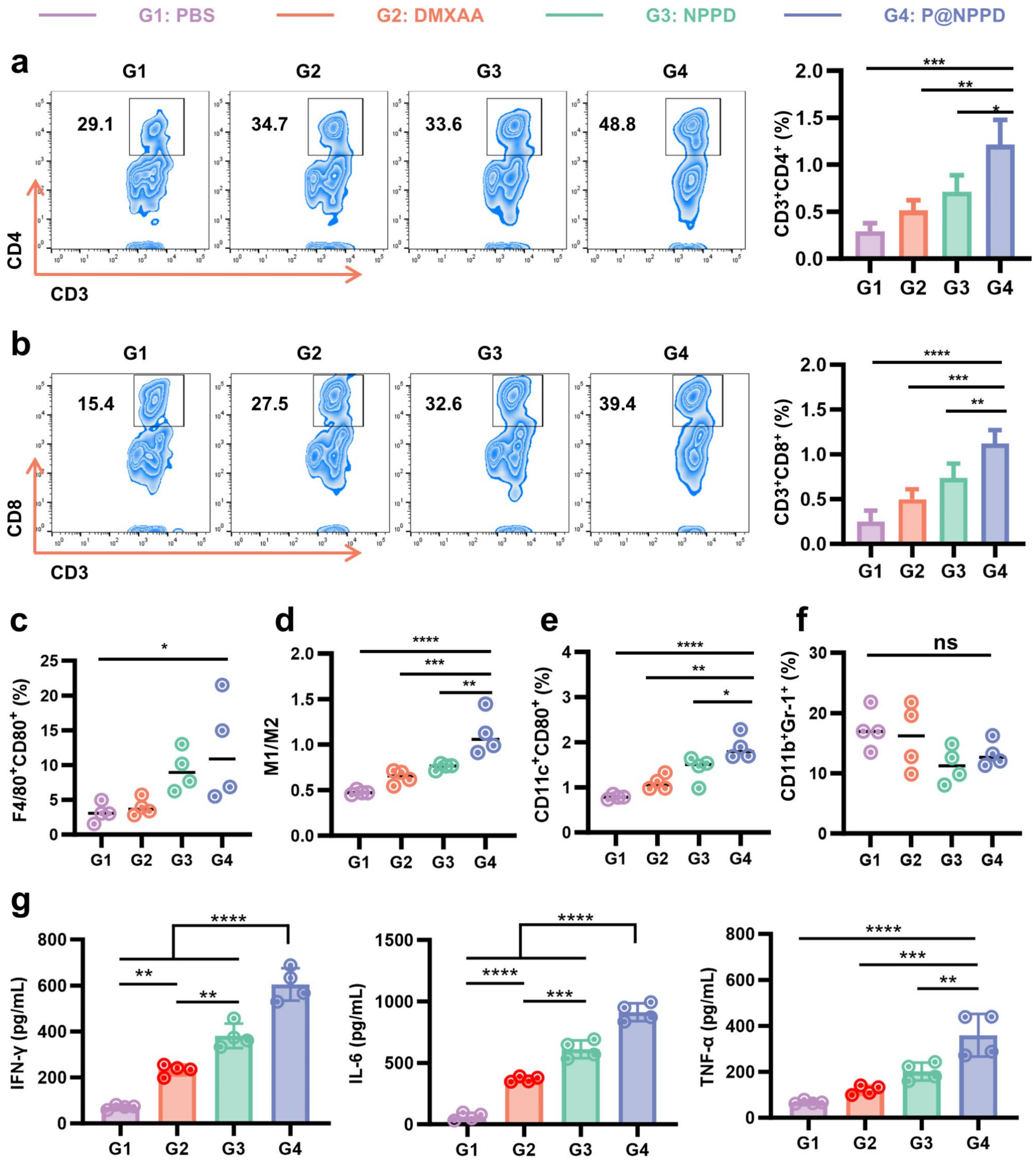

Fig. 5 Immune landscape of the tumor microenvironment as analyzed by flow cytometry. (**a**) Analysis of CD4$^+$ T-cell populations (CD3$^+$CD4$^+$ as a fraction of total single cells within the tumor) through flow cytometry. (**b**) Assessment of CD8$^+$ T cells (CD3$^+$CD8$^+$ as a percentage of total single cells in the tumor) through flow cytometry. (**c**) Evaluation of M1 macrophages (percentage of F4/80$^+$CD80$^+$ cells among all single cells) through flow cytometry. (**d**) Comparison of the ratio of M1 to M2 macrophages. (**e**) Measurement of activated dendritic cells (CD11c$^+$CD80$^+$ as a fraction of total single cells in the tumor). (**f**) Quantification of MDSCs (CD11b$^+$Gr-1$^+$ as a percentage of total single cells in the tumor, $n=4$). (**g**) Determination of the levels of cytokines, specifically IFN-γ, IL-6, and TNF-α, within tumors through ELISA. Groups: G1: PBS; G2: DMXAA; G3: NPPD; G4: P@NPPD. ns, not significant; *$p<0.05$, **$p<0.01$, ***$p<0.001$, ****$p<0.0001$.

microenvironment. This immune modulation synergizes with vascular blockade, enhancing antitumor efficacy.

To further evaluate immune activation, we quantified IFN-γ, IL-6, and TNF-α levels using enzyme-linked immunosorbent assay (ELISA) (Fig. 5g). Compared with the DMXAA group, NPPD treatment significantly elevated the levels of these antitumor cytokines, likely due to the nanoparticles' ability to extend drug half-life. Notably, P@NPPD treatment further amplified cytokine secretion, with IFN-γ increasing 1.58-fold, IL-6 by 1.49-fold, and TNF-α by 1.79-fold compared to NPPD alone. These results underscore P@NPPD's capacity for self-amplifying drug-targeted delivery and enhanced immune activation.

Besides, this study has some limitations. First, the single drug DMXAA was used, and future studies could explore combination therapies to achieve better efficacy. Second, P@NPPD still exhibits some degree of non-specific distribution in vivo, particularly accumulating in the liver and kidneys, which requires further optimization to enhance drug enrichment at tumor sites. Finally, this study was based on mouse models, whose tumor microenvironment differs from that of humans, necessitating further validation of efficacy and safety through larger animal models and clinical trials.

Conclusion

This study demonstrates the efficacy of a platelet-conjugated N_3-PEG-*b*-PHEA-DMXAA system for targeted cancer therapy. Leveraging platelets' tumor-homing properties and the coagulation cascade, the delivery system achieved a 2.61-fold increase in targeting efficiency and an 89.1% tumor suppression rate, significantly enhancing DMXAA localization and efficacy while reducing systemic toxicity. These findings present P@NPPD as a safe, precise, and promising platform for clinical cancer treatment.

Abbreviations

DLS	Dynamic light scattering
ELISA	Enzyme-linked immunosorbent assay
HE	Hematoxylin and eosin
MDSC	Myeloid-derived suppressor cell
MFI	Mean fluorescence intensity
PBS	Phosphate-buffered saline
ROP	Ring-opening polymerization
SEM	Scanning electron microscopy
TEM	Transmission electron microscopy
TSR	Tumor suppression rates
VDA	Vascular-disrupting agent

Supplementary Information

The online version contains supplementary material available at https://doi.org/10.1186/s12951-025-03262-9 .

Supplementary Material 1

Acknowledgements

This study was financially supported by the Ministry of Science and Technology of China (2022YFE0110200), the National Natural Science Foundation of China (52273157, 52073279, 52025035), Jilin province (20230508102RC), as well as the Youth Innovation Promotion Association of Chinese Academy of Sciences (2022224).

Author contributions

H.C., N.S., and Z.T.: conceptualization. H.C., Y.X., Y.S., M.S. and W.Z.: methodology, data collection and analysis. H.C. and N.S.: writing-original draft. N.S. writing-review and editing. X.F., N.S., and Z.T.: supervision. N.S., and Z.T.: funding. All authors reviewed the manuscript.

Funding

This study was financially supported by the Ministry of Science and Technology of China (2022YFE0110200), the National Natural Science Foundation of China (52273157, 52073279, 52025035), Jilin Province (20230508102RC), and the Youth Innovation Promotion Association of the Chinese Academy of Sciences (2022224).

Data availability

No datasets were generated or analysed during the current study.

Declarations

Ethics approval and consent to participate

In vivo antitumor studies were performed in mice bearing CT26 colorectal or 4T1 breast cancer cells, adhering to the Guide for the Care and Use of Laboratory Animals. All protocols were approved by the Animal Care and Use Committee of the Changchun Institute of Applied Chemistry, Chinese Academy of Sciences.

Competing interests

The authors declare no competing interests.

Author details

[1]Department of Gastrointestinal Colorectal and Anal Surgery, China-Japan Union Hospital of Jilin University, Changchun 130033, China
[2]Key Laboratory of Polymer Ecomaterials, Changchun Institute of Applied Chemistry, Chinese Academy of Sciences, Changchun 130022, China
[3]State Key Laboratory of Polymer Science and Technology, Changchun Institute of Applied Chemistry, Chinese Academy of Sciences, Changchun 130022, China
[4]Department of Thyroid, The Second Hospital of Jilin University, Changchun 130041, China

Received: 15 August 2024 / Accepted: 20 February 2025

References

1. Carmeliet P, Jain RK. Principles and mechanisms of vessel normalization for cancer and other angiogenic diseases. Nat Rev Drug Discov. 2011;10 6:417–27. https://doi.org/10.1038/nrd3455
2. Martínez-Reyes I, Chandel NS. Cancer metabolism: looking forward. Nat Rev Cancer. 2021;21 10:669–80. https://doi.org/10.1038/s41568-021-00378-6
3. Elia I, Haigis MC. Metabolites and the tumour microenvironment: from cellular mechanisms to systemic metabolism. Nat Metab. 2021;3 1:21–32. https://doi.org/10.1038/s42255-020-00317-z
4. Eelen G, Treps L, Li X, Carmeliet P. Basic and therapeutic aspects of angiogenesis updated. Circ Res. 2020;127 2:310–29. https://doi.org/10.1161/circresaha.120.316851
5. Siemann DW. The unique characteristics of tumor vasculature and preclinical evidence for its selective disruption by tumor-vascular disrupting agents. Cancer Treat Rev. 2011;37 1:63–74. https://doi.org/10.1016/j.ctrv.2010.05.001
6. Zhang C, Ni D, Liu Y, Yao H, Bu W, Shi J. Magnesium silicide nanoparticles as a deoxygenation agent for cancer starvation therapy. Nat Nanotechnol. 2017;12 4:378–86. https://doi.org/10.1038/nnano.2016.280
7. Chen X, Tang Q, Wang J, Zhou Y, Li F, Xie Y, Wang X, Du L, Li J, Pu J, et al. A DNA/DMXAA/Metal-organic framework activator of innate immunity for

boosting anticancer immunity. Adv Mater. 2023;35 15:e2210440. https://doi.org/10.1002/adma.202210440.

8. Wang D, Feng C, Xiao Z, Huang C, Chen Z, Fang W, Ma X, Wang X, Luo L, Hu K, Tao W. Therapeutic hydrogel for enhanced immunotherapy: A powerful combination of MnO2 nanosheets and vascular disruption. Nano Today. 2022;47:101673. https://doi.org/10.1016/j.nantod.2022.101673.
9. Corrales L, Glickman LH, McWhirter SM, Kanne DB, Sivick KE, Katibah GE, Woo SR, Lemmens E, Banda T, Leong JJ, et al. Direct activation of STING in the tumor microenvironment leads to potent and systemic tumor regression and immunity. Cell Rep. 2015;11 7:1018–30. https://doi.org/10.1016/j.celrep.2015.04.031
10. Weiss JM, Guérin MV, Regnier F, Renault G, Galy-Fauroux I, Vimeux L, Feuillet V, Peranzoni E, Thoreau M, Trautmann A. The STING agonist DMXAA triggers a Cooperation between T lymphocytes and myeloid cells that leads to tumor regression. 2017;6 10:e1346765; https://doi.org/10.1080/2162402X.2017.1346765
11. Chen X, Xu Z, Li T, Thakur A, Wen Y, Zhang K, Liu Y, Liang Q, Liu W, Qin JJ, Yan Y. Nanomaterial-encapsulated STING agonists for immune modulation in cancer therapy. Biomark Res. 2024;12(1:2). https://doi.org/10.1186/s40364-023-00551-z.
12. Liu Z, Zhang Y, Shen N, Sun J, Tang Z, Chen X. Destruction of tumor vasculature by vascular disrupting agents in overcoming the limitation of EPR effect. 2022;183:114138; https://doi.org/10.1016/j.addr.2022.114138
13. Hadi MK, Wang X, Peng Y, Sangaraju S, Ran F. Functional Polymeric Membrane Materials: A Perspective from Versatile Methods and Modification to Potential Applications.Polymer Science & Technology. 2024. https://doi.org/10.1021/polymscitech.4c00030
14. Nishihara H. Human pathological basis of blood vessels and stromal tissue for nanotechnology. Adv Drug Deliv Rev. 2014;74:19–27. https://doi.org/10.1016/j.addr.2014.01.005
15. Sun R, Xiang J, Zhou Q, Piao Y, Tang J, Shao S, Zhou Z, Bae YH, Shen Y. The tumor EPR effect for cancer drug delivery: current status, limitations, and alternatives. Adv Drug Deliv Rev. 2022;191:114614. https://doi.org/10.1016/j.addr.2022.114614.
16. Dai Q, Wilhelm S, Ding D, Syed AM, Sindhwani S, Zhang Y, Chen YY, MacMillan P, Chan W. Quantifying the ligand-coated nanoparticle delivery to cancer cells in solid tumors. ACS Nano. 2018;12 8:8423–35. https://doi.org/10.1021/acsnano.8b03900
17. Seidi K, Neubauer HA, Moriggl R, Jahanban-Esfahlan R, Javaheri T. Tumor target amplification: implications for nano drug delivery systems. 2018;275:142–61. https://doi.org/10.1016/j.jconrel.2018.02.020
18. Zhu Y, Gong P, Wang J, Cheng J, Wang W, Cai H, Ao R, Huang H, Yu M, Lin L, et al. Amplification of lipid peroxidation by regulating cell membrane unsaturation to enhance chemodynamic therapy. Angew Chem Int Ed Engl. 2023;62 12:e202218407. https://doi.org/10.1002/anie.202218407.
19. Zhu Y, Wang W, Gong P, Zhao Y, Pan Y, Zou J, Ao R, Wang J, Cai H, Huang H. Enhancing catalytic activity of a nickel single atom enzyme by polynary heteroatom doping for ferroptosis-based tumor therapy. 2023;17 3:3064–76; https://doi.org/10.1021/acsnano.2c11923
20. Wang Y, Shen N, Wang Y, Zhang Y, Tang Z, Chen X. Self-amplifying nanotherapeutic drugs homing to tumors in a manner of chain reaction. Adv Mater. 2021;33 7:e2002094. https://doi.org/10.1002/adma.202002094.
21. Pan H, Zheng M, Ma A, Liu L, Cai L. Cell/Bacteria-based bioactive materials for cancer immune modulation and precision therapy. Adv Mater. 2021;33 50:e2100241. https://doi.org/10.1002/adma.202100241.
22. Bush LM, Healy CP, Javdan SB, Emmons JC, Deans TL. Biological cells as therapeutic delivery vehicles. Trends Pharmacol Sci. 2021;42 2:106–18. https://doi.org/10.1016/j.tips.2020.11.008
23. Jia M, Miao W, Li Y, Guo Y, Zeng J, Gao Y, Li X, Wang Y, Zhao Z, Xu Z, et al. A polymerized probucol nanoformulation with neutrophil extracellular vesicle camouflage for cerebral ischemia-reperfusion injury therapy. Innov. 2024;100761. https://doi.org/10.1016/j.xinn.2024.100761.
24. He Y, Zhang S, She Y, Liu Z, Zhu Y, Cheng Q, Ji X. Innovative utilization of cell membrane-coated nanoparticles in precision cancer therapy. Exploration. 2024;4 6:20230164. https://doi.org/10.1002/EXP.20230164.
25. Ortiz-Otero N, Mohamed Z, King MR. Platelet-Based drug delivery for Cancer applications. Adv Exp Med Biol. 2018;1092:235–51. https://doi.org/10.1007/978-3-319-95294-9_12
26. Hu Q, Sun W, Wang J, Ruan H, Zhang X, Ye Y, Shen S, Wang C, Lu W, Cheng K, et al. Conjugation of Haematopoietic stem cells and platelets decorated with anti-PD-1 antibodies augments anti-leukaemia efficacy. Nat Biomed Eng. 2018;2 11:831–40. https://doi.org/10.1038/s41551-018-0310-2
27. Zanotelli MR, Reinhart-King CA. Mechanical forces in tumor angiogenesis. Adv Exp Med Biol. 2018;1092:91–112. https://doi.org/10.1007/978-3-319-95294-9_6
28. Aird WC. Endothelial cell heterogeneity. Cold Spring Harb Perspect Med. 2012;2(1):a006429. https://doi.org/10.1101/cshperspect.a006429.
29. Giannakeas V, Narod SA. Incidence of Cancer among adults with thrombocytosis in Ontario, Canada. JAMA Netw Open. 2021;4 8:e2120633. https://doi.org/10.1001/jamanetworkopen.2021.20633.
30. Mezouar S, Frère C, Darbousset R, Mege D, Crescence L, Dignat-George F, Panicot-Dubois L, Dubois C. Role of platelets in cancer and cancer-associated thrombosis: experimental and clinical evidences. Thromb Res. 2016;139:65–76. https://doi.org/10.1016/j.thromres.2016.01.006
31. Stefanini M, Dameshek W. Collection, preservation and transfusion of platelets; with special reference to the factors affecting the survival rate and the clinical effectiveness of transfused platelets. N Engl J Med. 1953;248 19:797-802. https://doi.org/10.1056/nejm195305072481901
32. Hu CM, Fang RH, Wang KC, Luk BT, Thamphiwatana S, Dehaini D, Nguyen P, Angsantikul P, Wen CH, Kroll AV, et al. Nanoparticle biointerfacing by platelet membrane cloaking. Nature. 2015;526 7571:118–21. https://doi.org/10.1038/nature15373
33. Silva-Santana G, Bax JC, Fernandes DCS, Bacellar DTL, Hooper C, Dias A, Silva CB, de Souza AM, Ramos S, Santos RA, et al. Clinical hematological and biochemical parameters in Swiss, BALB/c, C57BL/6 and B6D2F1 Mus musculus. Anim Model Exp Med. 2020;3 4:304–15. https://doi.org/10.1002/ame2.12139
34. Zhao M, Liu Y, Hsieh RS, Wang N, Tai W, Joo KI, Wang P, Gu Z, Tang Y. Clickable protein nanocapsules for targeted delivery of Recombinant p53 protein. J Am Chem Soc. 2014;136 43:15319–25. https://doi.org/10.1021/ja508083g
35. Chen H, Locke D, Liu Y, Liu C, Kahn ML. The platelet receptor GPVI mediates both adhesion and signaling responses to collagen in a receptor density-dependent fashion. J Biol Chem. 2002;277 4:3011–9. https://doi.org/10.1074/jbc.M109714200
36. Shi R, Zhang Z, Zhu A, Xiong X, Zhang J, Xu J, Sy MS, Li C. Targeting type I collagen for cancer treatment. Int J Cancer. 2022;151 5:665–83. https://doi.org/10.1002/ijc.33985
37. Ho-Tin-Noé B, Goerge T, Cifuni SM, Duerschmied D, Wagner DD. Platelet granule secretion continuously prevents intratumor hemorrhage. Cancer Res. 2008;68 16:6851–8. https://doi.org/10.1158/0008-5472.Can-08-0718
38. Rayes J, Watson SP. Platelet GPVI repairs its own damage. Blood. 2015;126 8:933–4. https://doi.org/10.1182/blood-2015-06-650838
39. Zhang L, Bo R, Wu Y, Li L, Zhu Z, Ma AH, Xiao W, Huang Y, Rojalin T, Yin X, et al. Programmable bispecific Nano-immunoengager that captures T cells and reprograms tumor microenvironment. Nano Lett. 2022;22 17:6866–76. https://doi.org/10.1021/acs.nanolett.2c00582
40. Ngo W, Ahmed S, Blackadar C, Bussin B, Ji Q, Mladjenovic SM, Sepahi Z, Chan WCW. Why nanoparticles prefer liver macrophage cell uptake in vivo. Adv Drug Deliv Rev. 2022;185:114238. https://doi.org/10.1016/j.addr.2022.114238.
41. Huang Y, Wang J, Jiang K, Chung EJ. Improving kidney targeting: the influence of nanoparticle physicochemical properties on kidney interactions. J Control Release. 2021;334:127–37. https://doi.org/10.1016/j.jconrel.2021.04.016
42. Liang J, Wang H, Ding W, Huang J, Zhou X, Wang H, Dong X, Li G, Chen E, Zhou F, et al. Nanoparticle-enhanced chemo-immunotherapy to trigger robust antitumor immunity. Sci Adv. 2020;6 35:eabc3646. https://doi.org/10.1126/sciadv.abc3646.
43. Downey CM, Aghaei M, Schwendener RA, Jirik FR. DMXAA causes tumor site-specific vascular disruption in murine non-small cell lung cancer, and like the endogenous non-canonical Cyclic dinucleotide STING agonist, 2′3′-cGAMP, induces M2 macrophage repolarization. PLoS ONE. 2014;9 6:e99988. https://doi.org/10.1371/journal.pone.0099988.

Publisher's note